Feasibility study of using desalination brine to control the stiffness and early-age hydration of 3D printable cementitious materials

Chen, Yu; Toosumran, Nuttapon; Chehab, Noura; Spanjers, Henri; Çopuroğlu, Oğuzhan

DOI
10.1016/j.jclepro.2022.134522

Publication date
2022

Document Version
Final published version

Published in
Journal of Cleaner Production

Journal of Cleaner Production 378 (2022) 134522

Contents lists available at ScienceDirect

Journal of Cleaner Production

journal homepage: www.elsevier.com/locate/jclepro

Feasibility study of using desalination brine to control the stiffness and early-age hydration of 3D printable cementitious materials

Yu Chen [a,*], Nuttapon Toosumran [a], Noura Chehab [b], Henri Spanjers [a], Oğuzhan Çopuroğlu [a,**]

[a] Faculty of Civil Engineering and Geosciences, Delft University of Technology, Delft, the Netherlands
[b] ENOWA (NEOM Energy & Water Company), NEOM, Saudi Arabia

ARTICLE INFO

Handling Editor: Zhen Leng

Keywords:
Desalination brine
3D concrete printing
Stiffness evolution
Early-age hydration
Calcined clay

ABSTRACT

This paper proposes the use of desalination brine as a setting and hydration activator in set-on-demand 3D concrete printing. A series of tests were conducted to investigate the effect of adding different concentrations of desalination brine on stiffness evolution and early-age hydration of Portland cement mortars (PC mixtures) and limestone-calcined clay-based cementitious materials (LC mixtures). Results show that, increasing brine concentration decreased slump, flowability and initial setting time, as well as enhanced buildability, and stimulated the stiffness development within the first hour. Furthermore, the addition of desalination brine resulted in an acceleration of cement hydration, a higher amount of chemically bound water and a higher 1st day compressive strength. The abovementioned behaviors were further promoted by doubling the brine concentration. Due to the presence of reactive aluminates in calcined clay, the acceleration of first-day hydration was slightly diminished and a higher intensity of Friedel's salt was observed in LC mixtures compared to that of PC mixtures with the same desalination brine addition.

1. Introduction

Increasing digitalization in building and construction industry is required to respond to the demand of creating a sustainable built environment (Bos et al., 2016; De Schutter et al., 2018; Wolfs et al., 2021). In this context, digital fabrication of concrete stands out as an ideal option for a technologically innovative, environmentally responsible and future-oriented solution (Chen et al., 2017). Over the last decades, extrusion-based 3D concrete printing (3DCP), as one of the most emerging and popular techniques in this field, received considerable attention and has been developed rapidly due to its benefits for rapid construction processes and unique architectural designs (Buswell et al., 2018; De Schutter et al., 2018). Also, 3DCP may be an environmentally-friendly approach to concrete manufacturing by using sustainable cementitious materials (Chen et al., 2017).

The 3DCP process can be explained as fresh cementitious filaments being extruded from a nozzle in a layer-based manner to form the designed objects without formwork (Mohan et al., 2020; Wolfs et al., 2019). Owing to the lack of formwork in 3DCP, the deposited fresh mortar/concrete filament must emerge with sufficient yield stress to restrain the deformation under the load from subsequent layers (Chen et al., 2020a; Perrot et al., 2016). Until now, there are two main strategies used in 3DCP, i.e., extrusion of high or sufficiently high stiffness material and set-on-demand printing (Mechtcherine et al., 2021). The former, as a very common approach used in many earlier works (Bai et al., 2021; Chen et al., 2021; Le et al., 2012; Ma et al., 2018; Nerella et al., 2019; Panda et al., 2019; Rahul et al., 2020; Weng et al., 2018), relies on the thixotropy nature of cementitious materials. The thixotropy of fresh mixture can be enhanced by adding a proper amount of silica fume (Nerella et al., 2019; Yuan et al., 2018), organic viscosity modifying admixture (Marchon et al., 2018), or nanoparticles, e.g., nano-clay (Kawashima et al., 2021; Moeini et al., 2020; Panda et al., 2019; Yuan et al., 2018), and nano-calcium carbonate (Chu et al., 2021; Yuan et al., 2018). However, the shortages of extruding thixotropy-based mixtures are the relatively high pumping pressure as well as the short printability window, which may hinder the implementation of this technology in a large-scale construction (Chen et al., 2021). In contrast, set-on-demand (hydration/rheology control) is reported as a more advanced and sophisticated approach (Anton et al., 2021; Boscaro et al., 2021; Reiter et al., 2020). The strategy usually comprises the use of fresh mixtures

* Corresponding author.
** Corresponding author.
E-mail addresses: Y.Chen-6@tudelft.nl (Y. Chen), O.Copuroglu@tudelft.nl (O. Çopuroğlu).

https://doi.org/10.1016/j.jclepro.2022.134522
Received 8 June 2022; Received in revised form 22 August 2022; Accepted 2 October 2022
Available online 7 October 2022

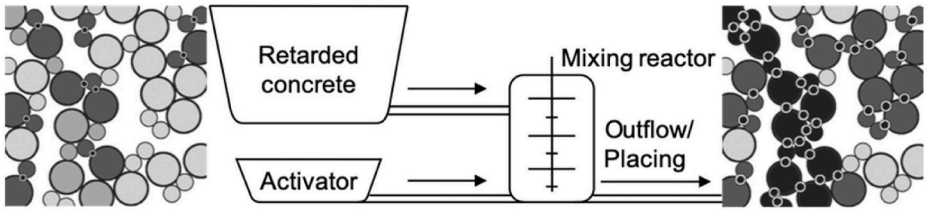

(a)

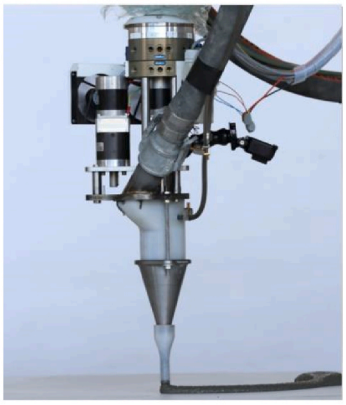

(b)

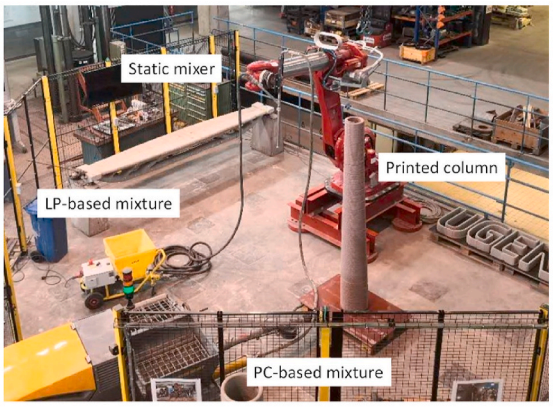

(c)

Fig. 1. (a) Schematic illustration of the set-on-demand 3DCP concept, adapted from (Reiter et al., 2020). The mixing reactor can be a dynamic mixer or a static mixer. (b) Printhead equipped with a dynamic mixer from ETH Zurich, adapted from (Reiter, 2019); (c) 3DCP setup equipped with a static mixer-based printhead from Ghent University, adapted from (Tao et al., 2021a).

with great fluidity, which will be transported to the nozzle and mixed with an activator (or accelerator) only when the materials are at the printhead, as shown in Fig. 1 (a).

As reported by Refs (Mechtcherine et al., 2020; Tao et al., 2021b), the printhead can be equipped with a dynamic mixer or a static mixer to mix fresh cementitious material and activator properly. The activator in set-on-demand printing can be an inorganic chemical accelerator, a kind of fast-set paste/mortar, or an organic viscosity modifying agent (Mechtcherine et al., 2021). The working mechanism of different activators has been reported elsewhere (Marchon et al., 2018). Aluminum sulfate salts-based shotcrete accelerator (Esnault et al., 2019) and calcium aluminate cement (CAC) paste (Anton et al., 2021; Boscaro et al., 2021; Reiter et al., 2020) were successfully employed as activators, which were dosed in the printhead incorporating a dynamic mixer (Fig. 1 (b)). Instead of dosing liquid or paste accelerators, Tao et al. (2021a) developed a mortar-based accelerator (consisting of fine sand, limestone powder, alkali-free shotcrete accelerator, and superplasticizer) that works perfectly on the 3D concrete printer equipped with a static mixer-based printhead (Fig. 1 (c)).

Desalination has been increasingly employed to meet the rising water demand in the last decade. About 15900 desalination plants are currently in operation worldwide (Jones et al., 2019). Desalination is defined as the process of producing freshwater that meets the requirements of human uses from saline water such as seawater, brackish water and brine (Darre and Toor, 2018; Panagopoulos and Haralambous, 2020). However, desalination brine (also known as reject brine, or brine in this paper) as the main by-product is also produced during the desalination process. Depending on the desalination type, 35%–45% of intake saline water can be converted into pure water, whereas the remaining (near 60%) is reject brine (Fattah et al., 2017). The composition of desalination brine is close to the intake saline water (seawater, brackish water, or brine), but it also contains additional chemicals used in the desalination process (Fattah et al., 2017; Panagopoulos and Haralambous, 2020). Desalination brine is usually discharged into marine or other surface water bodies, causing severe effects on the aquatic ecosystem (Jones et al., 2019; Meneses et al., 2010; Roberts et al., 2010). Therefore, brine disposal is an environmental challenge and eagerly needs sustainable solutions. Utilizing and stabilizing such a desalination brine into concrete has been proposed by (Fattah et al., 2017). The authors reported that using desalination brine (chloride concentration: 39426 mg/L) as the source of mixing water in blended cement (containing 50% of ground granulated blast-furnace slag) can potentially reduce CO_2 emission with more than 176 kg/m^3 of concrete produced.

Due to the very high chloride salt concentration, employing desalination brine as the source of mixing water in concrete may result in a rapid workability loss, which is not ideal for the mold-cast process of conventional concrete. Alternatively, many recent studies (Guo et al., 2020; Li et al., 2019, 2020; Liu et al., 2021; Ren et al., 2021; Shi et al., 2015; Wang et al., 2020) tried to use seawater containing relatively lower chloride ion concentration (9000–33400 mg/L). Typically, Cl^-, Na^+, SO_4^{2-}, Mg^{2+}, Ca^{2+}, and K^+ are the major ions in seawater (Li et al., 2021). Among them, chloride ion has the highest proportion and plays a vital role in cement setting and hydration (Li et al., 2021; Montanari et al., 2019). The effect of seawater on fresh properties of cement paste has been studied by (Li et al., 2019; Wang et al., 2020). Li et al. (2019) found that adding seawater can reduce workability, flowability and packing density, as well as increase cohesion of fresh cement paste. According to Wang et al. (2020, 2018), the negative effect on the fluidity of fresh cement paste is attributed to the increase in yield stress and viscosity caused by mixing with seawater. Li et al. (2020) reported that the early-age hydration of C_3S can be stimulated by seawater. Friedel's salt ($3CaO{\cdot}Al_2O_3{\cdot}CaCl_2{\cdot}10H_2O$) as a typical hydration product in the cement paste mixed with seawater is formed by the reaction between chloride ions and aluminate-ferrite-monosulfate (AFm). Furthermore, alumina-rich supplementary cementitious materials (SCMs), i.e., metakaolin and slag, were recommended in the cementitious composites with seawater/reject brine. The addition of reactive aluminate phases in

Table 1
Oxide composition of low-grade calcined clay (LGCC), limestone powder (LP), and Portland cement (PC).

XRF [wt.%]	PC	LP	LGCC
CaO	68.71	55.4	0.55
SiO_2	17.41	0.17	55.14
Al_2O_3	4.62	0.03	38.43
Fe_2O_3	2.75	0.04	2.60
K_2O	0.63	0	0.17
TiO_2	0.34	0	1.12
ZrO_2	0	0	0.05
Other	5.54	44.36	1.94
Total	100.00	100.00	100.00

cementitious materials can enhance the binding capacity of chloride to form more Friedel's salt, which may contribute to densifying the microstructure, improving mechanical performance and durability of hardened concrete at later ages (Cheng et al., 2018; Li et al., 2015, 2021; Shi et al., 2015).

For most mold-cast concrete applications, rapid acceleration of stiffness and early-age hydration may not be necessary, but it appears to be a major benefit to achieving the goal of set-on-demand printing. However, research to date has not yet determined the effect of desalination brine that has a much higher chloride concentration (>50000 mg/L) than seawater on fresh-state behaviors and hydration kinetics of cementitious materials. Moreover, to our knowledge, no research has attempted to use the desalination brine as an activator to accelerate the structural build-up of 3D printable cementitious materials. Therefore, in this paper, we propose using desalination brine as a setting and hydration accelerator in set-on-demand 3DCP.

This study aims to determine the feasibility of using desalinization brine as a chemical additive to control stiffness development and early-age hydration of 3D printable cementitious materials. The impacts of using desalination brine and concentrated brine on the flowability, stiffness evolution and hydration of Portland cement-based and limestone-calcined clay-based cementitious materials were investigated. For evaluating the fresh properties of studied mixtures, slump, slump flow, Vicat penetration resistance, plate-stacking and layer settlement tests were performed. In addition, isothermal calorimetry, thermogravimetric analysis, and X-ray diffraction analysis were carried out to characterize early-age hydration kinetics and phase assemblages of the resulting materials. Finally, compressive strength test (1, 3, and 7 days) was conducted to investigate the influence of adding desalination brine on the strength development of hardened cementitious materials during the first 7 days.

2. Material and methods

2.1. Materials

The binding materials used in this work were CEM I 52.5 Portland cement (PC), low-grade calcined clay (LGCC) and limestone powder (LP). LGCC that contained about 50% of metakaolin was purchased from Argeco, France. According to our earlier study (Chen et al., 2021), the reactive aluminate and silicate in LGCC are about 32 wt% and 12.3 wt%, respectively. Oxide composition obtained by X-ray fluorescence (XRF) spectrometry of PC, LGCC and LP is given in Table 1. Fig. 2 shows particle size distribution using laser diffractometry and X-ray diffraction (XRD) patterns of PC, LGCC and LP, obtained by A PhilipsPW1830 powder X-ray diffractometer with Cu-Kα radiation operated at 45 kV and

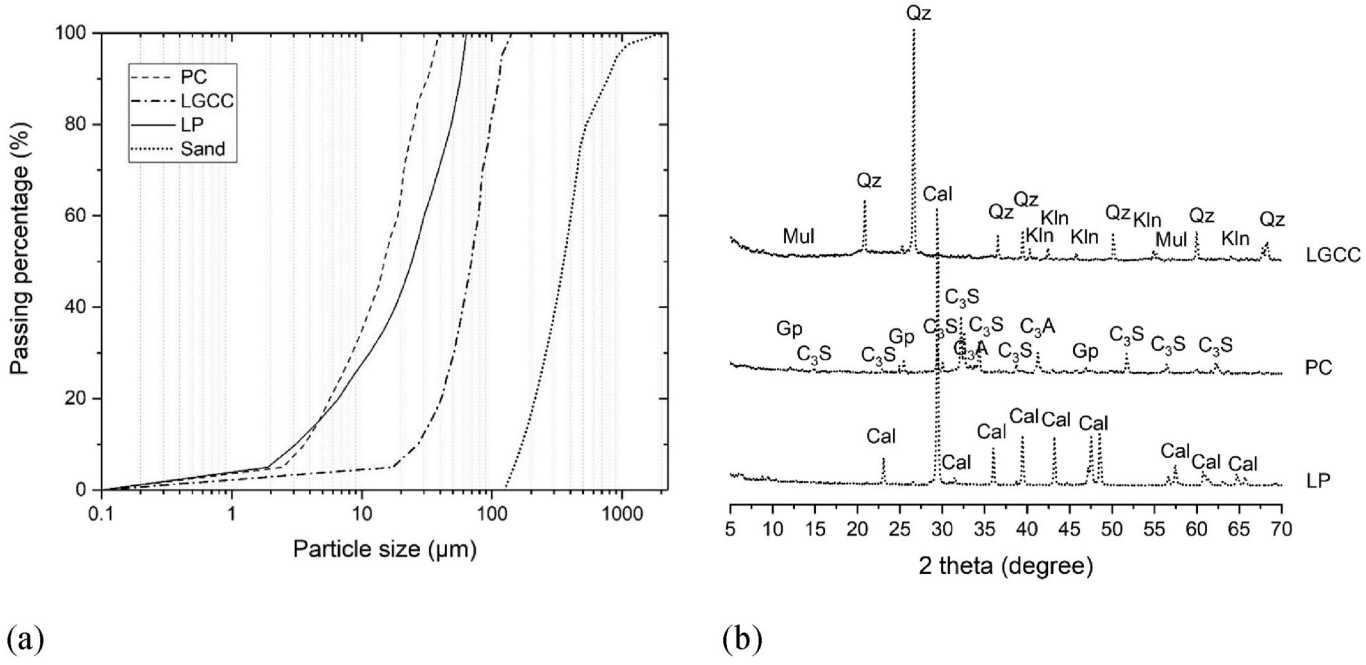

Fig. 2. (a) Particle size distribution of PC, LGCC, LP and quartz sand; (b) XRD (Cu-Kα radiation) patterns of LGCC, PC, and LP. Cal-calcite, Gp-gypsum, C_3S-alite, C_3A-tricalcium aluminate, Mul-mullite, Qz-quartz, Kln-kaolinite.

Table 2
Ion composition of Brine-1 and tap water.

Ions	Ca^{2+} (mg/L)	Na^{+} (mg/L)	Mg^{2+} (mg/L)	K^{+} (mg/L)	Cl^{-} (mg/L)	SO_4^{2-} (mg/L)	Others (mg/L)	Total dissolved solids (mg/L)	pH
Brine-1	21633	9941	3569	163	58227	87	173	93794	7.0
Tap water*	45	32	6.9	–	47	43	120	–	8.0

Tap water*: The ion composition of tap water is provided by Evides, the Netherlands.

Table 3
Mix designs of cementitious materials (wt.% of the binder mass).

	Mortar mixture						Brine mixture			
	Binder			Admixture	Water	Aggregate	Brine/tap water			Filler
	PC	LP	LGCC	SP	Tap Water	Sand (quartz)	Brine-1	Brine-2*	Tap Water	LP
P0	100	–	–	0.5	30	150	–	–	–	–
P1	100	–	–	0.5	30	150	–	–	40	180
P2	100	–	–	0.5	30	150	40	–	–	180
P3	100	–	–	0.5	30	150	–	40	–	180
C0	55	15	30	1	30	150	–	–	–	–
C1	55	15	30	1	30	150	–	–	40	180
C2	55	15	30	1	30	150	40	–	–	180
C3	55	15	30	1	30	150	–	40	–	180

Brine-2*: The concentration of all ions is about twice that of Brine-1.

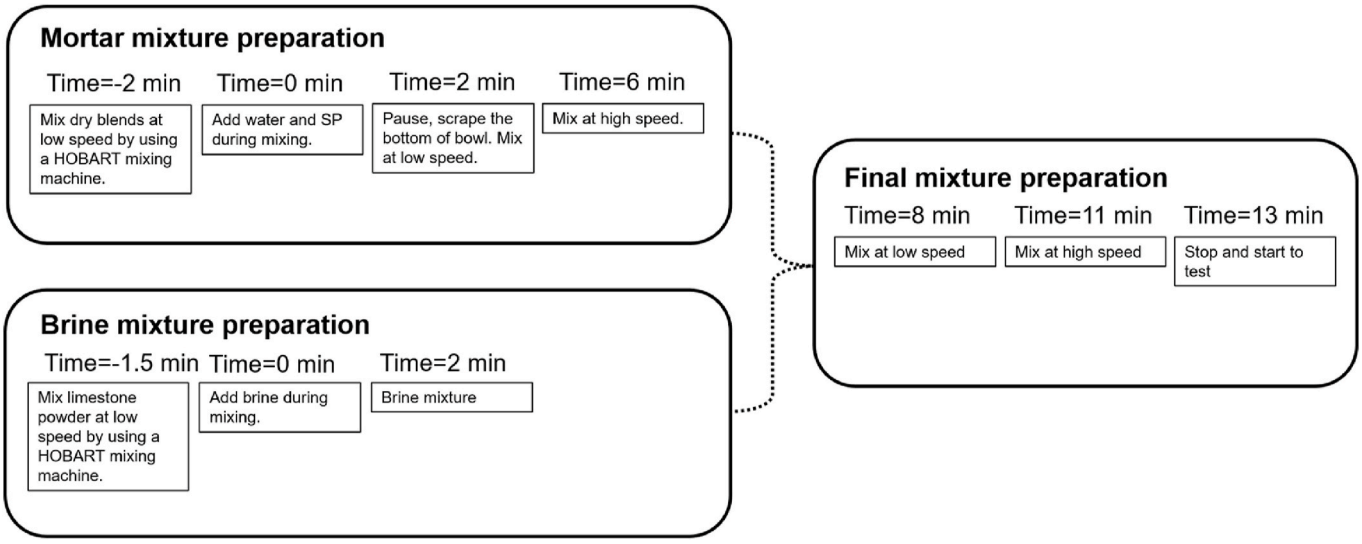

Fig. 3. Mixing protocol for the fresh mixture preparation.

40 mA. As shown in Fig. 2 (b), quartz is the main impurity of LGCC. Fine quartz sand with 0.125–2 mm grain size was employed as aggregate. The chemical composition of the desalination brine (Brine-1) used in this study that was analyzed in Waterlab (TU Delft) is reported in Table 2. The cations and anions were assessed by Inductively Coupled Plasma-Mass Spectrometry (ICP-MS) (Plasma Quant MS, Analytik Jena, Germany), and Ion Chromatograph (IC) (Metrohm 881-IC compact pro, Switzerland), respectively. It was found that the main cation and anion were Ca^{2+} and Cl^{-}, respectively. The chemical composition of tap water supplied by Evides, the Netherlands, is also presented in Table 2.

For a set-on-demand printing system, the printable cementitious material with two components, i.e., a mortar mixture and an injectable activator, needs to be developed. The mortar mixture was employed as the base for the final printable material. The brine mixture containing normal or high concentration brine was designed as an injectable activator to stimulate stiffness evolution and hydration of the mortar mixture. Both mixtures were mixed inline in the printhead. Thus, mortar and brine mixtures were prepared separately and then mixed to make the final mixture. Table 3 presents the mix designs of different mixtures studied in this work. Except for mixtures P0 and C0, all mixtures were combinations of mortar and brine mixtures in a mass ratio of 1.27. For mortar mixtures, there are two groups, i.e., Portland cement-based materials (PC mixtures) and limestone-calcined clay-based cementitious materials. (LC mixtures). The binder of the LC mixtures consisted of 55 wt% PC, 15 wt% LP, and 30 wt% LGCC. The aggregate-to-binder ratio and water-to-binder ratio were selected as 1.5 and 0.3. To adjust flowability to satisfy the requirements for pumping, 0.5–1 wt% of polycarboxylate ether (PCE)-based superplasticizer (SP) was added to mortar mixtures. Following the preliminary slump flow test, mixture P0 (0.5 wt% of SP) showed a similar spread diameter (about 175 mm) compared to that of mixture C0 (1 wt% of SP). The initial setting time of mixtures P0 and C0 were 146 min and 161 min, respectively. Mixtures containing calcined clay need a high SP dosage to reach the desired workability, which can be attributed to the adsorption of PCEs into the amorphous structure of metakaolin particles (Ferreiro et al., 2017). Please note that mixtures P0 and C0 were only the mortar part of PC (P1–P3) and LC (C1–C3) mixtures. Thus, their behaviors were not discussed in the Result section. For brine mixtures, there were three liquid options, i.e., tap-water (reference), Brine-1, and Brine-2. In this study, Brine-2 was defined as a concentrated brine with nearly two times higher salinity than Brine-1. Brine-2 was obtained by heating Brine-1 at 68 °C to evaporate the excess volume of water. Note that directly injecting brine into the mortar mixture will rapidly increase the total liquid-to-solid ratio, potentially affecting the buildability of deposited layers in the 3DCP process. Thus, LP as the filler was mixed with tap-water/brine in a mass ratio of 4.5. The final mixture was the combination of fresh mortar and brine mixtures, which were prepared separately. Instructions for the mixing protocol can be found in Fig. 3. The time zero (T = 0 min) in this paper was defined as the time of mixing liquid suspension (water + SP or brine) with dry materials.

2.2. Test procedures

2.2.1. Evaluation of fresh state behaviors

Slump and slump flow tests were employed at the material age of 15–20 min to assess the shape retention and flowability of the studied

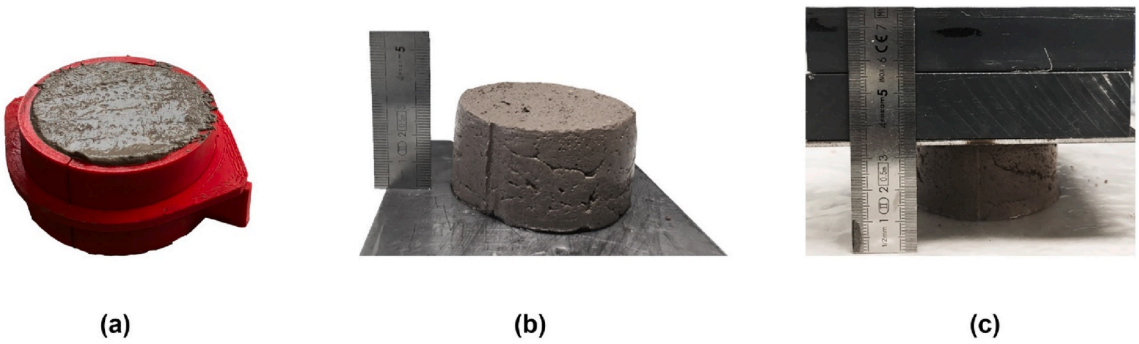

Fig. 4. Illustration of the plate-stacking test process: (a) Cast cylindrical sample with customized ABS mold; (b) Measure the height of demolded sample; (c) Place static loads on the top of demolded sample.

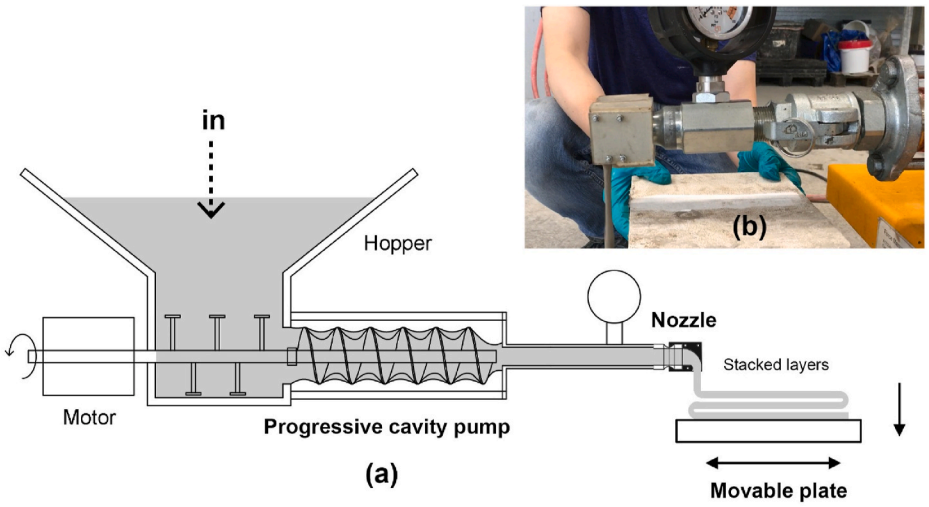

Fig. 5. Illustration of layer settlement test process: (a) Schematic section of the extrusion setup containing a progressive cavity pump, a nozzle with a rectangle opening and a manually controlled movable plate; (b) Photograph of the rectangle nozzle, extruded filament and manually controlled movable plate.

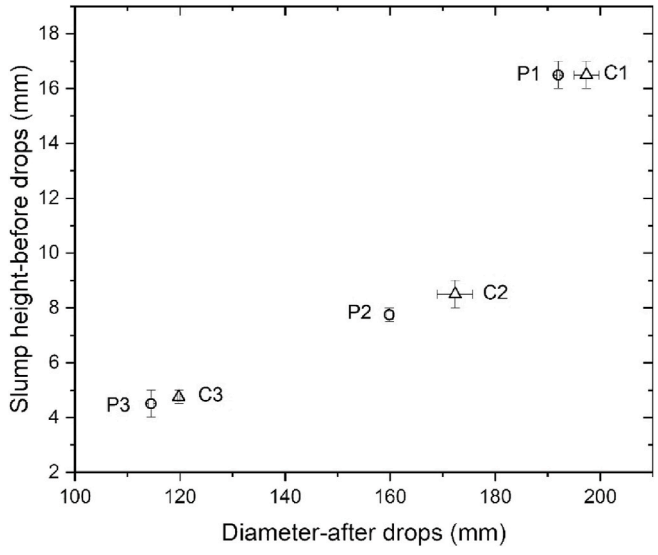

Fig. 6. Slump and slump flow test results.

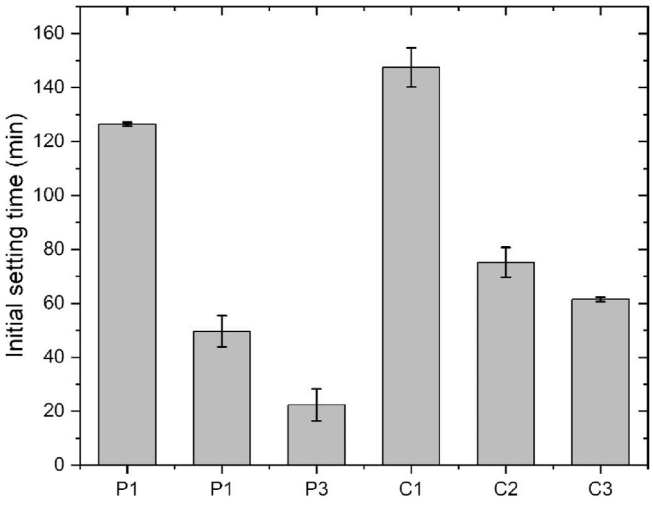

Fig. 7. Initial setting time of studied mixtures.

mixtures. Hägermann cone was used to perform both tests. The test protocol followed the recommendation of (Chen et al., 2021). The slump value and spread diameter (25 times of table drops) can effectively indicate the buildability and pumpability of fresh mixtures (Chen et al., 2020a, 2021; Tay et al., 2019). Meanwhile, the initial setting time of all mixtures was measured by an automatic Vicat machine. The fresh sample was tested following the specifications of NEN-EN 196-3 (2016). Additionally, the plate-stacking test (Chen et al., 2021; Kazemian et al., 2017; Panda et al., 2017; Perrot et al., 2016) was conducted at 15 min, 30 min, 45 min, and 60 min to determine the evolution of stiffness/green

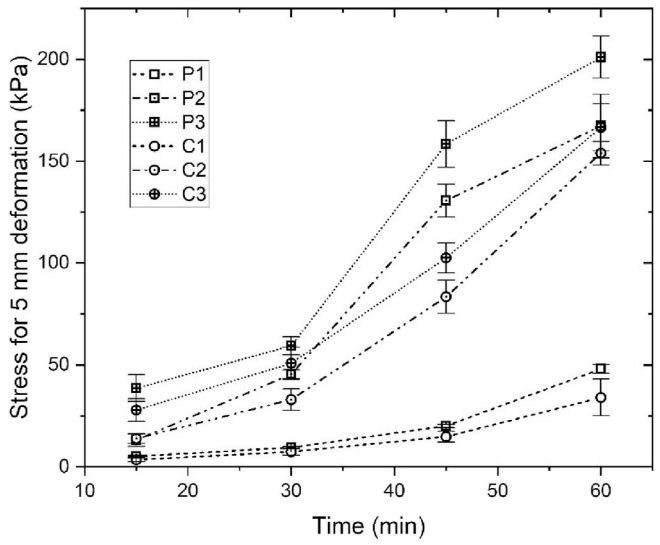

Fig. 8. Results of the plate-stacking test.

strength. As shown in Fig. 4, cylindrical samples were cast using a 3D printed acrylonitrile butadiene styrene (ABS) mold (height: 35 mm; internal diameter: 60 mm). Before filling the fresh mixtures, mold oil was applied to coat the mold's interior surface for easily demolding. Static load (plates) was gradually placed on the demolded sample until the vertical deformation reached 5 ± 1 mm. The maximum load was defined as the green strength of the sample at a specific material age. Note that this test aimed to compare the stiffness of different mixtures at the same resting time, rather than assessing the exact value of green strength.

To investigate the impacts of adding brine on buildability, mixtures C1 and C2 were selected to perform a layer settlement test (Kazemian et al., 2017). A nozzle with a rectangle opening (13.5 mm in height and 40 mm in width) was attached to a PFT Swing M conveying pump (also known as progressive cavity pump) for extruding filaments on a manually controlled movable plate (see Fig. 5). A straight wall was manufactured by stacking filaments. Each layer only contains one filament with a dimension of 40 mm (width) × 13.5 mm (height) × 245 mm (length). The maximum number of stacked layers before collapsing was regarded as the indicator of buildability performance. About 8 L of fresh mixture was prepared for conducting this test. The pumping rate of the layer settlement test was 40 rpm, and the test was performed at the material age of 20 min.

2.2.2. Characterization of early-age hydration

Isothermal calorimetry test was performed in an eight-channel TAM Air isothermal calorimeter to quantify the hydration heat released during the first 7 days. Fresh pastes were prepared by following the same procedure. The pre-mixed liquid containing water, SP and brine was poured into the pre-weighed dry components (binder + LP filler), and then the mixture was stirred manually for 2 min. Afterward, 6 g of fresh paste was filled into a 20 mL glass vessel. The sample and reference vessels were placed in the calorimeter under 20 °C. Paste samples were also used for the thermogravimetric analysis (TGA) and qualitative X-ray diffraction (XRD) analysis. Cylindrical specimens with the dimension of 33.5 mm in diameter and 67.5 mm in height were cast and stored in a fog room (>99% relative humidity, 20 ± 2 °C) up to the time of stop hydration (4 h, 20 h, and 7 days). The hydration of pastes samples was stopped using solvent exchange method with isopropanol (see (Chen et al., 2020b; Lothenbach et al., 2016)). Netzsch STA 449 F3 Jupiter was used for TGA. With a heating rate of 10 °C/min, about 50 mg of powder sample was heated from 40 to 900 °C. The whole test was in an argon environment with a 30 mL/min flow rate. XRD patterns of different paste samples were determined using PhilipsPW1830 powder X-ray diffractometer, with Cu-Kα radiation operated at 45 kV and 40 mA. The diffraction angle (2θ) was in the range of 5°–70°.

40 mm cubic samples were cast and tested at 1, 3, and 7 days to monitor the compressive strength development. All specimens were stored in the fog room (>99% relative humidity, 20 ± 2 °C) until the compressive strength test was conducted. A loading rate of 2.4 kN/s was selected to perform the compression test following NEN-EN 196-1 (2016). The compressive strength of each mixture at each age was obtained by three repeated tests.

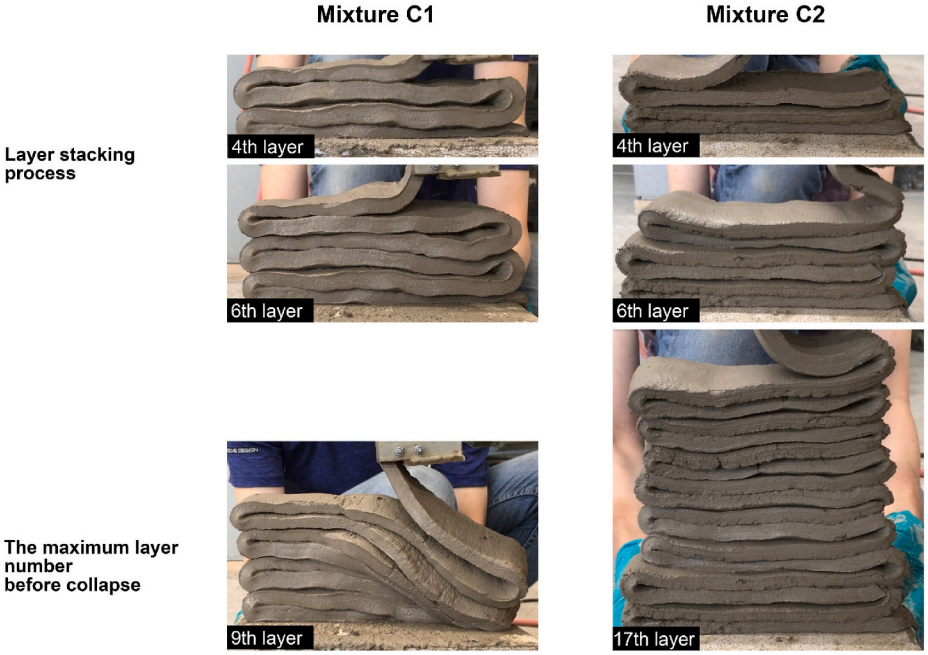

Fig. 9. Photographs of layer settlement test.

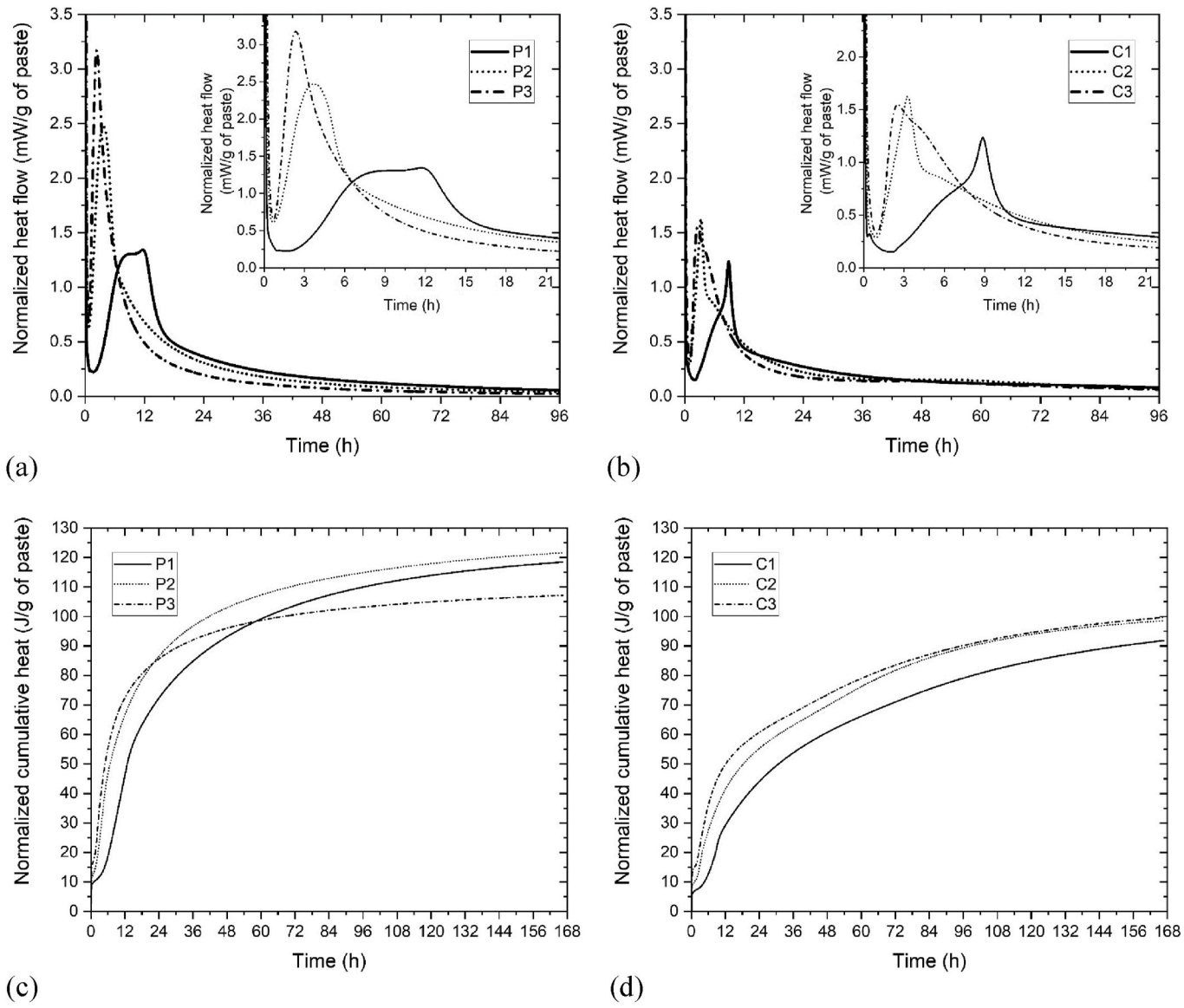

Fig. 10. Isothermal calorimetry test results: (a) Mixtures P1, P2, and P3-normalized heat flow with time; (b) Mixtures C1, C2, and C3-normalized heat flow with time; (c) Mixtures P1, P2, and P3-normalized cumulative heat with time; (d) Mixtures C1, C2, and C3-normalized cumulative heat with time.

3. Results and discussion

3.1. Fresh state behaviors

3.1.1. Slump and slump flow

The slump and slump-flow test results of the studied mixtures are presented in Fig. 6. Both slump height before table drops and spread diameter after table drops were decreased by adding desalination brine. Both values were further reduced by doubling the brine concentration. Compared to LC mixtures, PC mixtures exhibited slightly lower flowability with the same brine mixture due to the lower dosage of SP addition.

3.1.2. Stiffness development

As shown in Fig. 7, the initial setting time was decreased by using desalination brine. The reduction of the initial setting time was more than 70 min. Increasing the brine concentration further reduced the initial setting time. The acceleration of the initial set for PC mixtures was much more evident than that of LC mixtures. Fig. 8 shows the plate-stacking test results of the studied mixtures. All fresh mixtures became stiffer over time. The addition of desalination brine remarkably accelerated the structural build-up of fresh samples. Increasing brine concentration further enhanced this effect, which agreed with the initial setting time test results. This is because the increase in ion concentration in the mixing water can enhance particle flocculation and ionic strength (Wang et al., 2018), as well as accelerate the process of pore solution saturation and crystal precipitation, resulting in an internal structure with high cohesion and rapid hardening.

Furthermore, with the same brine mixture, PC mixtures showed a lower flowability, a higher stiffness at the same resting time and a shorter initial setting time than LC mixtures. This may be attributed to the relatively high SP dosage in mixtures C1, C2, and C3. According to earlier studies (Chen et al., 2021; Gelardi and Flatt, 2015; Mantellato et al., 2019), increasing PCEs content (before reaching the saturation dosage) can reduce yield stress and severely delay the nucleation and structuration processes of fresh cementitious materials.

3.1.3. Layer settlement

Only mixtures C1 and C2 were selected to perform the layer settlement test in this study. Fig. 9 compares the maximum stacked-layer

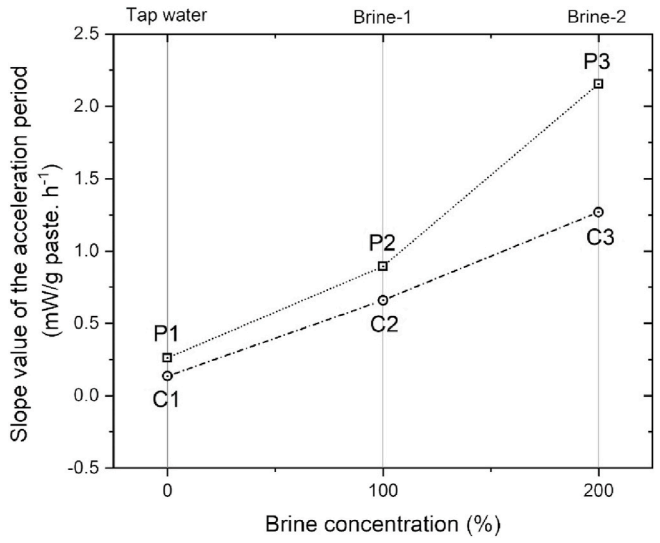

Fig. 11. Brine concentration as a function of the slope value of the acceleration period.

number before structure collapse using different mixtures. It can be found that more layers were deposited by using mixture C2 compared to mixture C1. The mixture incorporating desalination brine showed much better shape stability and buildability than the mixture with tap water, which was consistent with the results of slump and slump flow and plate-stacking tests. This confirmed that using brine mixture as an activator in the set-on-demand 3D printing process is feasible from a material perspective. However, it must be noted that our current setup cannot enable an inline mixing process. Further validation will be provided in future research.

3.2. Early age hydration and compressive strength

3.2.1. Isothermal calorimetry

Fig. 10 shows the normalized heat flow (96 h) and cumulative heat (7 days) of different paste mixtures obtained by isothermal calorimetry tests. As shown in Fig. 10 (a)(b), mixtures with desalination brine (P2, P3, C2, and C3) show a shorter induction period and required time to the main hydration peak, and a much higher intensity of the main hydration peak, compared to the mixtures with tap water (P1 and C1). Also, doubling the brine concentration can further enhance most of the abovementioned phenomena. Fig. 11 shows that the slope of the acceleration period was significantly increased by adding concentrated brine. Overall, the enhancement of hydration induced by brine is much more effective in PC mixtures than in LC mixtures. The curve pattern of mixtures incorporating brine in Fig. 10 (a)(b) is very close to that of Portland cement and pure $CaCl_2$ or commercial $CaCl_2$-based accelerator in Ref (Shanahan et al., 2016), since Cl^- and Ca^{2+} are the major ions in the brine used.

The intensity of the main hydration peak and the cumulative hydration heat in Fig. 10 were decreased by replacing part of PC with the blend of LF and LGCC (mixtures C1, C2, and C3). The slope of the acceleration period in LC mixtures was also lower than that of the PC mixtures, which can be attributed to the dilution effect of the high volume of PC replacement in the mixture. Additionally, for LC mixtures, many chloride ions may be immobilized through reaction with metakaolin (from LGCC) and cement (Li et al., 2015), leading to the reduction of slope in the acceleration period. Sulfate depletion was also observed in mixtures P1, C1, C2, and C3. A shoulder appeared after the main hydration peak in mixture P1 and C3. A narrow main hydration peak was observed in mixtures C1 and C2 due to the overlap of C_3S and aluminate peaks, in agreement with (Marchon and Flatt, 2015; Zingg et al., 2009). For mixtures P2 and P3, adding desalination brine can avoid the formation of such an aluminate peak. This may be attributed to sulfate ion in the brine (see Table 2), which can react with C_3A to form Ettringite and/or Monosulfate. However, due to the presence of reactive aluminate phases in LGCC (32 wt%), the aluminate peak cannot be eliminated even by adding concentrated brine in this work.

As shown in Fig. 10 (c), mixture P3 showed higher accumulated heat than mixtures P1 and P2 within the first 21 h. After that, the increment of cumulative heat of mixture P3 became smaller. At 7 days, mixture P2 had the maximum cumulative heat value in this group, whereas the gap between mixtures P1 and P2 gradually decreased since the second day of hydration. In contrast to PC mixtures, LC mixtures demonstrated a different trend in Fig. 10 (d). The cumulative heat value increased with increasing brine concentration, but there was little difference between mixtures C2 and C3 at 7 days.

3.2.2. Thermogravimetric and X-ray diffraction analysis

Thermogravimetric (TG) and derivative thermogravimetric (DTG) curves of different studied paste mixtures at 4 h, 20 h and 7 days of curing are presented in Fig. 12. A large peak around 100 °C in all DTG curves is induced by dehydration of Ettringite and water loss of C–S–H gel layers (Li et al., 2020; Liu et al., 2021). According to (Li et al., 2020; Liu et al., 2021; Lothenbach et al., 2016), the peak at 125–200 °C in DTG curves may be the decomposition peak of Friedel's salt for mixtures with desalination brine, whereas this peak is also considered as the mass loss of Monocarboaluminate (Mc) for mixtures P1 and C1, which was confirmed by our XRD results (see Fig. 14). Moreover, a small peak at about 300 °C may also indicate the formation of Friedel's salt (De Weerdt et al., 2019; Lothenbach et al., 2016; Lu et al., 2021) in mixtures P2, P3, C2, and C3. As shown in Fig. 12, at the same material age and brine concentration, the C–S–H and Ettringite peak intensity in LC mixtures was slightly lower. In contrast, the intensity of Mc and/or Friedel's salt peak was higher than that in PC mixtures.

According to Refs (Chen et al., 2020b; Lothenbach et al., 2016; Roychand et al., 2016), the amount of chemically bound water (H) can be computed from the mass loss in the temperature range of 40–600 °C (see Eq (1)). The decomposition temperature of calcium hydroxide (CH) is in the range of 400–500 °C. The CH content was calculated using Eq (2).

$$W_{[H_2O]} = \frac{M_{40^\circ C} - M_{600^\circ C}}{M_{600^\circ C}} \times 100\ (\%) \tag{1}$$

$$W_{[Ca(OH)_2]} = \frac{M_{400^\circ C} - M_{500^\circ C}}{M_{600^\circ C}} \times \frac{m_{[Ca(OH)_2]}}{m_{[H_2O]}} \times 100\ (\%) \tag{2}$$

where $W_{[H_2O]}$ and $W_{[Ca(OH)_2]}$ represent the mass percentages of H and CH in mixtures, respectively; $M_{40^\circ C}$, $M_{400^\circ C}$, $M_{500^\circ C}$ and $M_{600^\circ C}$ denote the TG results at 40 °C, 400 °C, 500 °C, and 600 °C; $m_{[Ca(OH)_2]}$, and $m_{[H_2O]}$ are the molar masses of CH (74 g/mol) and water (18 g/mol). The calcite content of each sample was also quantified, and we found little or no carbonation in our samples (details can be found in Appendix).

The computed H and CH contents are plotted in Fig. 13. In comparison with PC mixtures, LC mixtures showed much lower H and CH contents within the first 7 days because of the dilution effect induced by a high PC replacement. For PC mixtures, the highest H and CH amounts at 4 h were found in mixture P3. Afterward, mixtures P1 and P2 showed steeper H and CH growth than mixture P3. The highest H and CH percentages at 7 days were found in mixtures P2 and P1. The reduction of CH at 7 days in mixtures with desalination brine (P2 and P3) can be attributed to the formation of Friedel's salt (Liu et al., 2021). Increasing brine concentration can increase the chloride ion concentration to stimulate this process. However, for mixtures with LGCC and LF, mixtures containing desalination brine displayed a much higher H content than the mixture with tap water. The magnitude difference between mixtures C2 and C3 was small and gradually decreased. In Fig. 13 (b), the CH content in mixture C1 was the lowest at 4 h, but it became higher

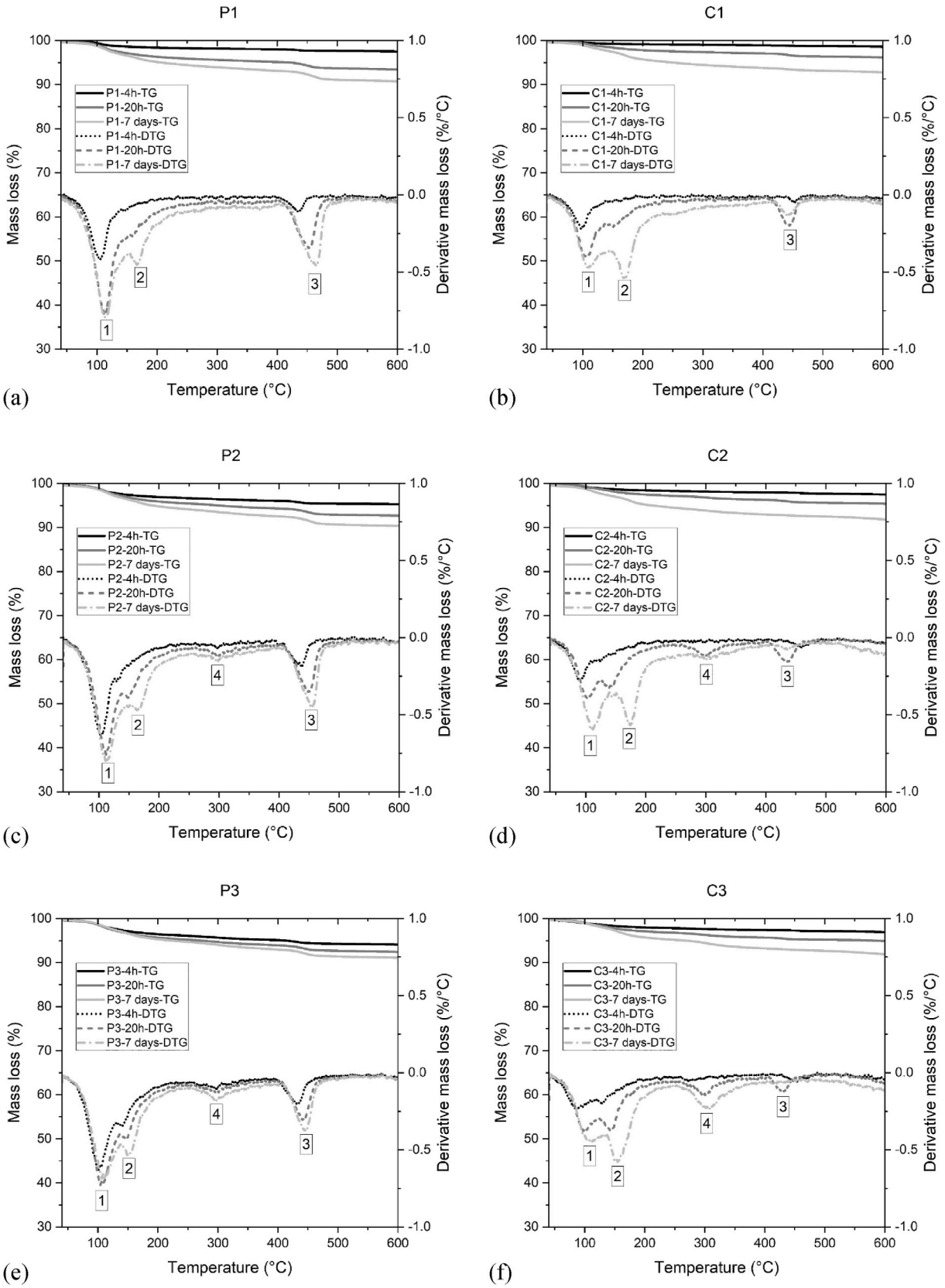

Fig. 12. TGA at 4 h, 20 h, and 7 days: (a) TG and DTG curves of mixture P1; (b) TG and DTG curves of mixture C1; (c) Mixture P2-TG and DTG curves; (d) TG and DTG curves of mixture C2; (e) TG and DTG curves of mixture P3; (f) TG and DTG curves of mixture C3. 1 – C–S–H and Ettringite, 2 – Monocarboaluminate and/or Friedel's salt, 3 – Portlandite, 4 – Friedel's salt.

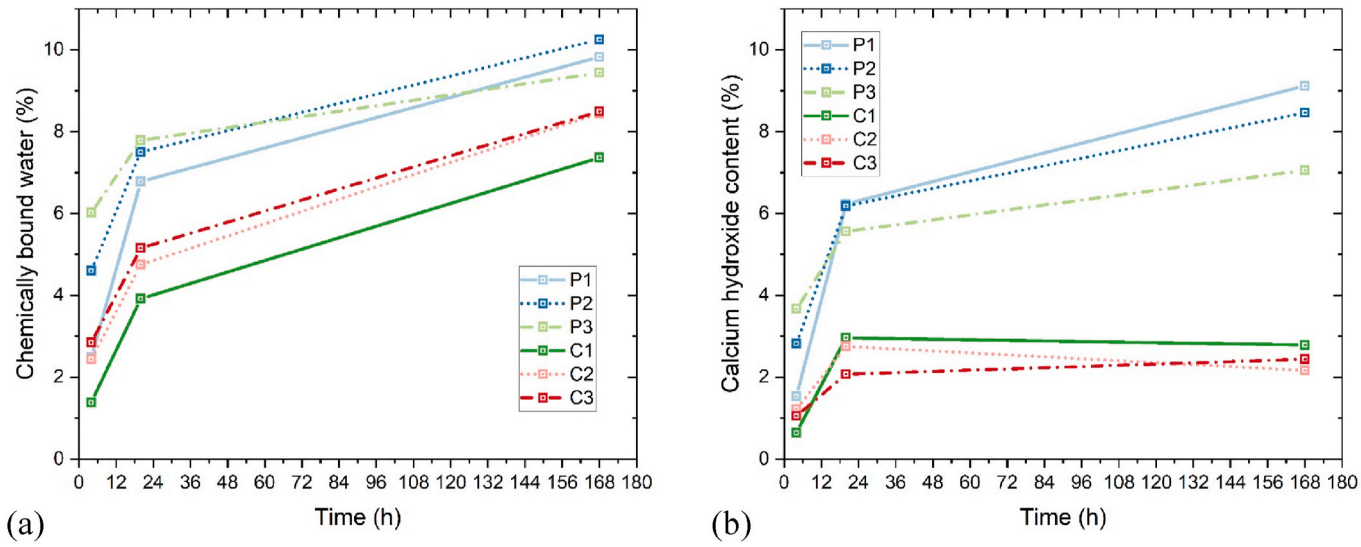

Fig. 13. (a) The normalized amount of chemically bound water (H), relative to the dry sample weight at 600 °C; (b) The normalized amount of Portlandite (CH), relative to the dry sample weight at 600 °C.

than in mixtures C2 and C3 from 20 h onwards. Besides, a slight reduction of CH percentage in mixtures C1 and C2 was also observed. The decrease of Portlandite may be related to the pozzolanic reaction caused by reactive aluminates in calcined clay, as described in (Chen et al., 2020b; Shi et al., 2015). Compared to PC mixtures, more AFm phases appeared to form in LC mixtures, which can bind more chloride ions, resulting in an increase in Friedel's salt at 7 days.

The finding in the TGA can be confirmed by the qualitative XRD analysis. As shown in Fig. 14, the presence of Friedel's salt was the main difference between mixtures with tap water and brine after 20 h of hydration. Friedel's salt peak intensity increased in both PC and LC mixtures with desalination brine from 20 h to 7 days. Instead of Friedel's salt, Mc as the main AFm appeared in mixtures C1 and P1 at 7 days. Compared to PC mixtures, larger amounts of Friedel's salt (mixtures with brine) and Mc (mixture with tap water) seemed to be formed in LC mixtures, which agreed with the results of (Shi et al., 2017). They found that the metakaolin can provide additional aluminates to promote the formation of Friedel's salt.

3.2.3. *Compressive strength*

Fig. 15 presents the compressive strength test results of different studied mixtures at 1, 3, and 7 days. PC mixtures showed much higher compressive strength than LC mixtures for the same brine concentration, indicating the dilution effect as discussed in Section 3.2.1. Furthermore, the 1st day compressive strength of PC and LC mixtures increased with increasing brine concentration, whereas the high brine concentration adversely affected the strength development of PC mixtures after the 1st day hydration. The compressive strength of mixture P1 at 3 and 7 days was very close to that of mixture P2 and higher than that of mixture P3. In contrast, mixtures C2 and C3 exhibited a stronger compressive strength than mixture C1 at 3 and 7 days. For LC mixtures, the side effect of increasing brine concentration on the 7-day compressive strength was limited. Similar values were found in mixtures C2 and C3.

Fig. 16 (a) illustrates a good linear correlation (R-squared: about 0.96) between normalized cumulative heat from the isothermal calorimetry and chemically bound water content from the TGA. Both can indicate early-age cement hydration. Assuming that all cast samples in this study had the same air void content, the compressive strength appeared to be dominated by the hydration of cementitious materials (Chen et al., 2020b, 2021). As shown in Fig. 16 (b), a positive correlation between compressive strength and normalized cumulative heat was found. The R-squared of the fitted curve was 0.95, which confirmed the critical role of cement hydration degree on compressive strength.

Overall, adding desalination brine accelerated and enhanced the first-day cement hydration and compressive strength of PC and LC mixtures. The acceleration and enhancement were further increased by increasing brine concentration. These effects were probably governed by the major ions in the brine, i.e., Cl^-, and Ca^{2+}. As summarized by Ref (Li et al., 2020), the abundant Cl^- can significantly stimulate the hydration of C_3S (see Eq (3)). During the cement hydration process, $CaCl_2$ (or $MgCl_2$) reacts with CH to form and precipitate calcium oxychloride (3Ca $(OH)_2$ $CaCl_2$ $12H_2O$) (Farnam et al., 2015; Li et al., 2020).

$$CaCl_2 + 3Ca(OH)_2 + 12H_2O \rightarrow 3Ca(OH)_2 \bullet CaCl_2 \bullet 12H_2O \quad (3)$$

This process can largely consume CH resulting in the reduction of alkalinity and Ca^{2+} concentration in the pore solution. The dissolution and hydration of C_3S are therefore promoted (Li et al., 2020).

However, doubling the brine concentration for PC mixture (P3) appeared to inhibit the cement hydration after the first day, resulting in a weaker compressive strength at 3 and 7 days compared to mixture P2. As shown in Fig. 12 (c) (e), mixture P3 displayed much weaker C–S–H and Ettringite intensity than in mixture P2 at 7 days. Also, the amount of portlandite and chemically bound water (7 days) and the cumulative heat (after the first day) in mixture P3 were lower than that of mixture P2 (see Figs. 10 (c) and 13). This may be attributed to the insufficient water available for later age hydration. A large amount of water may be consumed in mixture P3 within the first day due to the precipitation of large amounts of crystals caused by the high concentration brine (Brine-2). However, this hypothesis still needs to be confirmed in further research. As mentioned earlier, the compressive strength within the first 7 days was strongly dominated by the cement hydration. Therefore, the negative effect of high concentration brine (Brine-2) on cement hydration after the first day played a dominant role in the decrease in compressive strength of mixture P3 at 7 days. Increasing brine concentration also increased the concentration of many unfavorable ions, e.g., Mg^{2+}. The high concentration of Mg^{2+} in Brine-2 may have deleterious effects on the micro-mechanical performance of C–S–H, leading to strength degradation (Sun et al., 2022), which might also be a reason for the weak compressive strength of mixture P3 at 3 and 7 days. However, based on the current results, the deleterious effects induced by unfavorable ions are uncertain, and it requires further investigation.

Additionally, the calcium, aluminate and ferrite ions in pore solution may have been consumed to form Friedel's salt (C_3A/C_4AF $CaCl_2$ $12H_2O$) at the beginning of the cement hydration (see Eq (4)), which accelerated the hydration of C_3A, and C_4AF (Li et al., 2021).

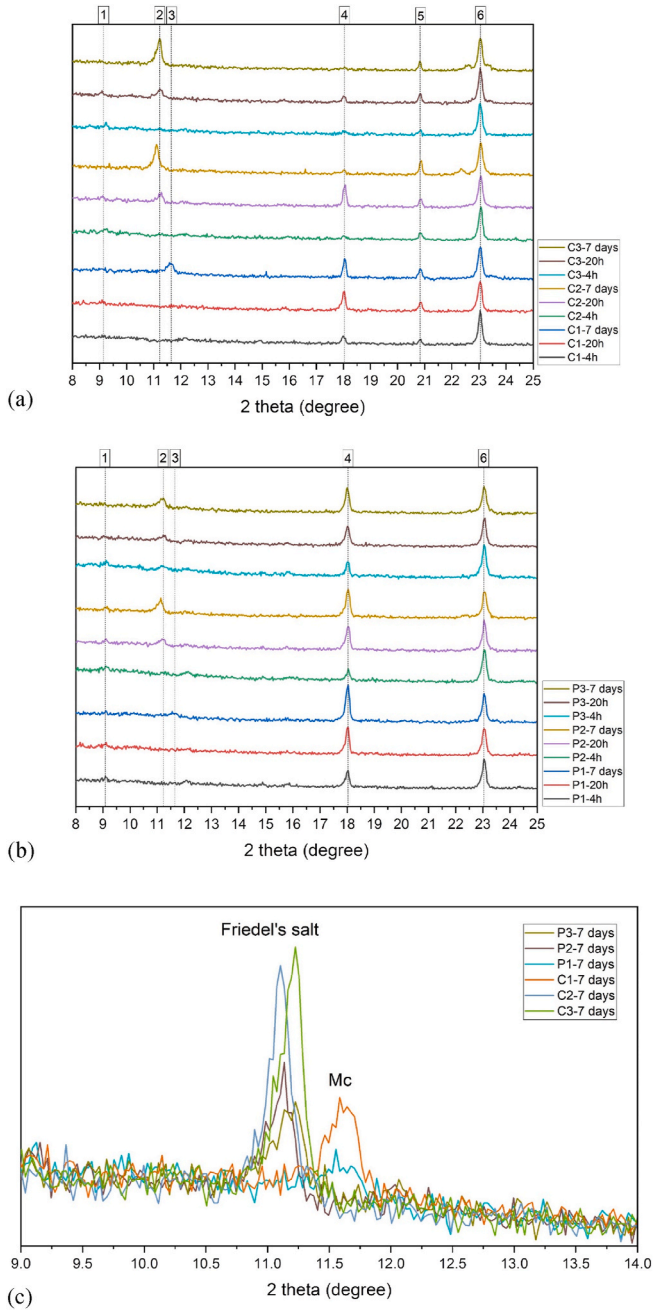

Fig. 14. (a) XRD results of mixtures C1, C2, and C3 at 4 h, 20 h, and 7 days; (b) XRD results of mixtures P1, P2, and P3 at 4 h, 20 h, and 7 days; (c) Comparison of Friedel's salt and Monocarboaluminate (Mc) intensities at 7 days. 1 – Ettringite, 2 – Friedel's salt, 3 – Monocarboaluminate, 4 – Portlandite, 5 – Quartz, 6 – Calcite.

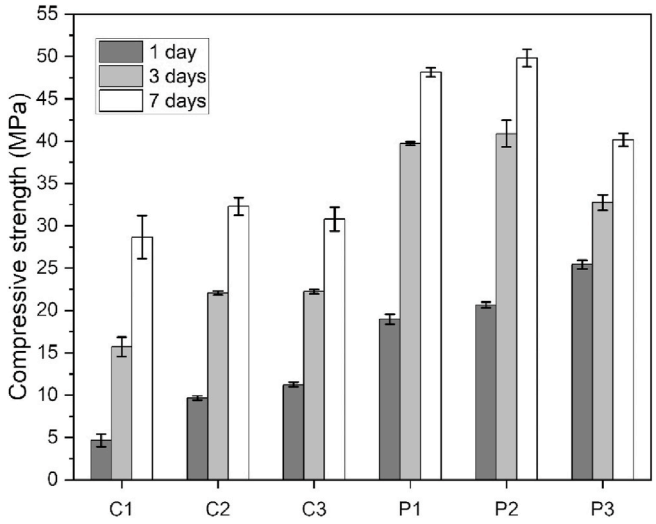

Fig. 15. Compressive strength of different mixtures at 1, 3, and 7 days.

related to the increase in Friedel's salt. Mixture C3 showed similar amounts of portlandite and chemically bound water as well as the cumulative heat at 7 days compared to mixture C2. Therefore, the cement hydration of mixture C3 did not appear to be adversely affected by Brine-2. This is also confirmed by the similar 7 days compressive strength between mixtures C2 and C3 (Fig. 15). As mentioned in Section 3.2.2., due to the presence of reactive aluminates (metakaolin) in LGCC, more Portlandite appeared to be consumed to form AFm and/or Friedel's salt. According to (Li et al., 2018, 2020), Friedel's salt can densify the microstructure of the cement matrix, improving the compressive strength. This might explain the relatively higher compressive strength at 3 and 7 days observed in mixtures C2 and C3 compared to mixture C1.

4. Conclusion

This paper aimed to investigate the effect of adding desalination brines at two different concentrations on fresh-state behaviors and early-age hydration of 3D printable cementitious materials. Both Portland cement mixtures and limestone-calcined clay-based cementitious materials were employed in this study. The results are summarized as follows.

- Increasing the brine concentration decreased flowability and initial setting time, as well as enhanced buildability and the stiffness evolution (within the first 1 h after water addition) of fresh mixture. By using the same brine mixture, PC mixtures demonstrated much weaker flowability and higher stiffness than LC mixtures. This phenomenon can be attributed to the high superplasticizer dosage and the dilution effect caused by high PC substitution in LC mixtures.
- For the 1st day of hydration, mixtures incorporating brine showed a shorter induction period, a higher slope of the acceleration period, a higher intensity of the main hydration peak, a shorter time to reach the main hydration peak, higher chemically bound water content and compressive strength compared to mixtures with tap water. Doubling the brine concentration further enhanced these behaviors. Additionally, compared to PC mixtures, the acceleration of first-day hydration was slightly diminished in LC mixtures, because the

$$C_3A \,/\, C_4AF + 2NaCl + Ca(OH)_2 + 10H_2O \rightarrow C_3A \,/\, C_4AF \bullet CaCl_2 \bullet 10H_2O + 2NaOH \quad (4)$$

Increasing chloride ion concentration (desalination brine concentration) further enhanced this acceleration and formed more Friedel's salt (Figs. 11, 12 and 14). As shown in Fig. 12 (d) and (f), mixture C3 exhibited a lower C–S–H and Ettringite intensity but a higher Friedel's salt intensity. The decrease in C–S–H and Ettringite intensity may be

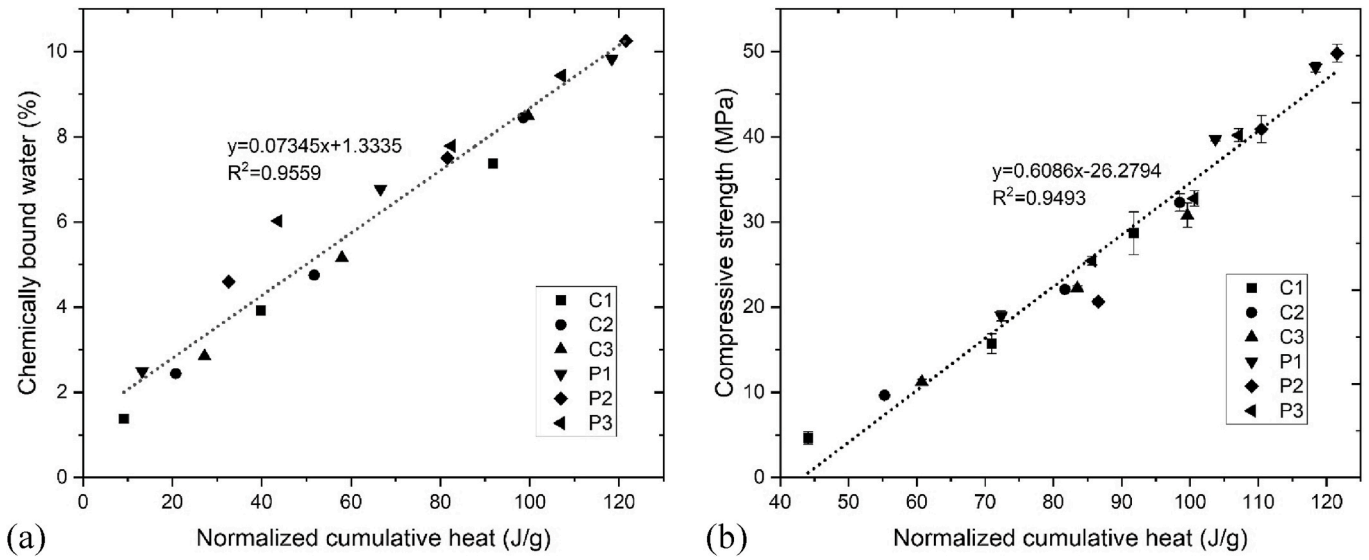

Fig. 16. The linear relationship between normalized cumulative heat by mass of paste and (a) Chemically bound water content; (b) Compressive strength.

reactive aluminates from LGCC may immobilize chloride ions at the beginning of the cement hydration.

- Except for mixture P3, the cumulative hydration heat and chemically bound water content at 7 days increased with increasing brine concentration. A strong correlation between the compressive strength of cast samples and the normalized cumulative heat from isothermal calorimetry was found. This indicated the dominant role of cement hydration on the compressive strength of cast samples.
- Adverse effects on cement hydration and compressive strength by adding concentrated brine were observed in mixture P3. However, such influences were not apparent in LC mixtures. Due to the presence of reactive aluminates (metakaolin) in LGCC, more Portlandite appeared to be consumed to form AFm and/or Friedel's salt at 7 days.
- The use of desalination brine or concentrated desalination brine as an activator in the context of set-on-demand 3DCP is feasible from a material point of view. However, the 3D printability of developed mixtures was not verified using a set-on-demand printing setup in this work. Furthermore, the mixing time employed in the current study appeared to be unnecessarily long. Therefore, in further research, a shorter mixing time (e.g., 10–30 s) will be employed, and the final mixture will also be prepared and assessed using a dynamic/static inline mixing system.

CRediT authorship contribution statement

Yu Chen: Conceptualization, Methodology, Investigation, Formal analysis, Data curation, Supervision, Writing – original draft, Writing – review & editing. **Nuttapon Toosumran:** Investigation, Validation, Formal analysis, Writing – review & editing. **Noura Chehab:** Conceptualization, Writing – review & editing. **Henri Spanjers:** Resources, Supervision, Writing – review & editing. **Oğuzhan Çopuroğlu:** Conceptualization, Supervision, Project administration, Funding acquisition, Writing – review & editing.

Declaration of competing interest

The authors declare that they have no known competing financial interests or personal relationships that could have appeared to influence the work reported in this paper.

Data availability

Data will be made available on request.

Acknowledgments

The authors would like to thank Mr. Arjan Thijssen for his support of the XRD. The second author would like to acknowledge the scholarship provided by the Siam Cement Public Company Limited (SCG) for MSc study at TU Delft and wants to thank Mr. Hamed Rastegarianjahromi for his help in determining the brine composition. Finally, the authors would like to thank the water supply team at NEOM for their support.

Appendix

According to (Lothenbach et al., 2016), the decomposition temperature of carbonation phases is in the range of 600–900 °C. If we assumed all the carbonation phases are calcite ($CaCO_3$), the calcite content was calculated using Eq (a1).

$$W_{[CaCO_3]} = \frac{M_{600^\circ C} - M_{900^\circ C}}{M_{600^\circ C}} \times \frac{m_{[CaCO_3]}}{m_{[CO_2]}} \times 100\ (\%) \quad \text{(a1)}$$

where $W_{[CaCO_3]}$ represents the mass percentages of calcite in mixtures; $M_{600^\circ C}$ and $M_{900^\circ C}$ denote the TG results at 600 °C, and 900 °C; $m_{[CaCO_3]}$, and $m_{[CO_2]}$ are the molar masses of calcite (100 g/mol) and CO_2 (44 g/mol). Figure A1 shows the TGA results and computed calcite content in all studied mixtures at 4 h, 20 h, and 7 days. It can be found that the measured calcite content is very close to that of the limestone powder content in the raw materials (binder + filler). Small fluctuations may be attributed to unavoidable deviations during the sample extraction. Thus, these results can confirm little or no carbonation in our samples.

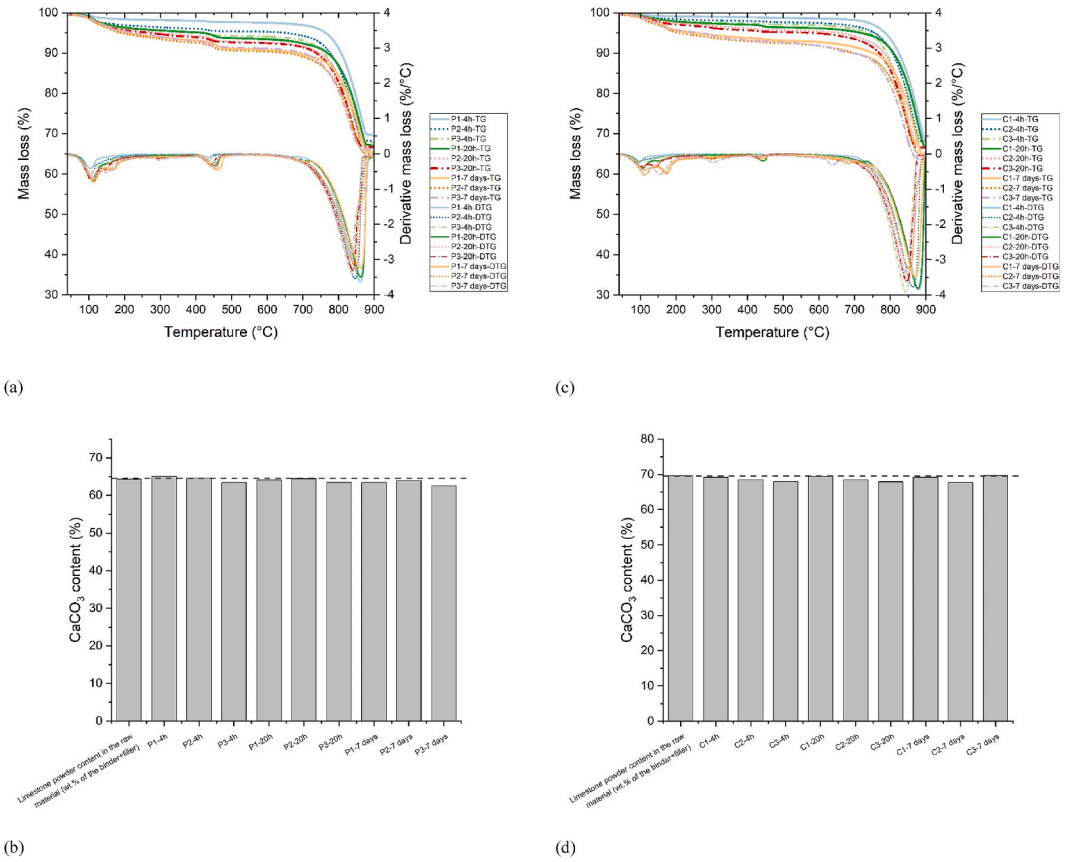

Fig. A1. (a) TGA results (40–900 °C) of mixtures P1, P2 and P3: TG and DTG curves at 4 h, 20 h, and 7 days; (b) The computed calcite amount of mixtures P1, P2 and P3 at 4 h, 20 h, and 7 days using Eq (a1); (c) TGA results (40–900 °C) of mixtures C1, C2 and C3: TG and DTG curves at 4 h, 20 h, and 7 days; (d) The computed calcite amount of mixtures C1, C2 and C3 at 4 h, 20 h, and 7 days using Eq (a1)..

References

Anton, A., Reiter, L., Wangler, T., Frangez, V., Flatt, R.J., Dillenburger, B., 2021. A 3D concrete printing prefabrication platform for bespoke columns. Autom. ConStruct. 122, 103467 https://doi.org/10.1016/j.autcon.2020.103467.

Bai, G., Wang, L., Ma, G., Sanjayan, J., Bai, M., 2021. 3D printing eco-friendly concrete containing under-utilised and waste solids as aggregates. Cem. Concr. Compos. 120, 104037 https://doi.org/10.1016/j.cemconcomp.2021.104037.

Bos, F., Wolfs, R., Ahmed, Z., Salet, T., 2016. Additive manufacturing of concrete in construction: potentials and challenges of 3D concrete printing. Virtual Phys. Prototyp. 11, 209–225. https://doi.org/10.1080/17452759.2016.1209867.

Boscaro, F., Quadranti, E., Wangler, T., Mantellato, S., Reiter, L., Flatt, R.J., 2021. Eco-friendly, set-on-demand digital concrete. 3D Print. Addit. Manuf. https://doi.org/10.1089/3dp.2020.0350.

Buswell, R.A., Leal de Silva, W.R., Jones, S.Z., Dirrenberger, J., 2018. 3D printing using concrete extrusion: a roadmap for research. Cement Concr. Res. 112, 37–49. https://doi.org/10.1016/j.cemconres.2018.05.006.

Chen, Y., Chaves Figueiredo, S., Li, Z., Chang, Z., Jansen, K., Çopuroğlu, O., Schlangen, E., 2020a. Improving printability of limestone-calcined clay-based cementitious materials by using viscosity-modifying admixture. Cement Concr. Res. 132, 106040 https://doi.org/10.1016/j.cemconres.2020.106040.

Chen, Y., He, S., Zhang, Y., Wan, Z., Çopuroğlu, O., Schlangen, E., 2021. 3D printing of calcined clay-limestone-based cementitious materials. Cement Concr. Res. 149, 106553 https://doi.org/10.1016/j.cemconres.2021.106553.

Chen, Y., Rodriguez, C.R., Li, Z., Chen, B., Çopuroğlu, O., Schlangen, E., 2020b. Effect of different grade levels of calcined clays on fresh and hardened properties of ternary-blended cementitious materials for 3D printing. Cem. Concr. Compos. 114, 103708 https://doi.org/10.1016/j.cemconcomp.2020.103708.

Chen, Y., Veer, F., Çopuroğlu, O., 2017. A critical review of 3D concrete printing as a low CO 2 concrete approach. Heron 62, 167–194.

Cheng, S., Shui, Z., Sun, T., Huang, Y., Liu, K., 2018. Effects of seawater and supplementary cementitious materials on the durability and microstructure of lightweight aggregate concrete. Construct. Build. Mater. 190, 1081–1090. https://doi.org/10.1016/j.conbuildmat.2018.09.178.

Chu, S.H., Li, L.G., Kwan, A.K.H., 2021. Development of extrudable high strength fiber reinforced concrete incorporating nano calcium carbonate. Addit. Manuf. 37, 101617 https://doi.org/10.1016/j.addma.2020.101617.

Darre, N.C., Toor, G.S., 2018. Desalination of water: a review. Curr. Pollut. Reports 4, 104–111. https://doi.org/10.1007/s40726-018-0085-9.

De Schutter, G., Lesage, K., Mechtcherine, V., Nerella, V.N., Habert, G., Agusti-Juan, I., 2018. Vision of 3D printing with concrete — technical, economic and environmental potentials. Cement Concr. Res. https://doi.org/10.1016/j.cemconres.2018.06.001.

De Weerdt, K., Lothenbach, B., Geiker, M.R., 2019. Comparing chloride ingress from seawater and NaCl solution in Portland cement mortar. Cement Concr. Res. 115, 80–89. https://doi.org/10.1016/j.cemconres.2018.09.014.

Esnault, V., Labyad, A., Chantin, M., Toussaint, F., 2019. Experience in online modification of rheology and strength acquisition of 3D printable mortars. In: Wangler, T., Flatt, R. (Eds.), First RILEM International Conference on Concrete and Digital Fabrication – Digital Concrete. Springer International Publishing, pp. 24–38. https://doi.org/10.1007/978-3-319-99519-9_3.

Farnam, Y., Dick, S., Wiese, A., Davis, J., Bentz, D., Weiss, J., 2015. The influence of calcium chloride deicing salt on phase changes and damage development in cementitious materials. Cem. Concr. Compos. 64, 1–15. https://doi.org/10.1016/j.cemconcomp.2015.09.006.

Fattah, K.P., Al-Tamimi, A.K., Hamweyah, W., Iqbal, F., 2017. Evaluation of sustainable concrete produced with desalinated reject brine. Int. J. Sustain. Built Environ. 6, 183–190. https://doi.org/10.1016/j.ijsbe.2017.02.004.

Ferreiro, S., Herfort, D., Damtoft, J.S., 2017. Effect of raw clay type, fineness, water-to-cement ratio and fly ash addition on workability and strength performance of calcined clay – limestone Portland cements. Cement Concr. Res. 101, 1–12. https://doi.org/10.1016/j.cemconres.2017.08.003.

Gelardi, G., Flatt, R.J., 2015. Working Mechanisms of Water Reducers and Superplasticizers, Science and Technology of Concrete Admixtures. Elsevier Ltd. https://doi.org/10.1016/B978-0-08-100693-1.00011-4.

Guo, M., Hu, B., Xing, F., Zhou, X., Sun, M., Sui, L., Zhou, Y., 2020. Characterization of the mechanical properties of eco-friendly concrete made with untreated sea sand and seawater based on statistical analysis. Construct. Build. Mater. 234, 117339 https://doi.org/10.1016/j.conbuildmat.2019.117339.

Jones, E., Qadir, M., van Vliet, M.T.H., Smakhtin, V., Kang, S. mu, 2019. The state of desalination and brine production: a global outlook. Sci. Total Environ. 657, 1343–1356. https://doi.org/10.1016/j.scitotenv.2018.12.076.

Kawashima, S., Wang, K., Ferron, R.D., Kim, J.H., Tregger, N., Shah, S., 2021. A review of the effect of nanoclays on the fresh and hardened properties of cement-based materials. Cement Concr. Res. 147, 106502 https://doi.org/10.1016/j.cemconres.2021.106502.

Kazemian, A., Yuan, X., Cochran, E., Khoshnevis, B., 2017. Cementitious materials for construction-scale 3D printing: laboratory testing of fresh printing mixture. Construct. Build. Mater. 145, 639–647. https://doi.org/10.1016/j.conbuildmat.2017.04.015.

Le, T.T., Austin, S.A., Lim, S., Buswell, R.A., Gibb, A.G.F., Thorpe, T., 2012. Mix design and fresh properties for high-performance printing concrete. Mater. Struct. Constr. 45, 1221–1232. https://doi.org/10.1617/s11527-012-9828-z.

Li, H., Farzadnia, N., Shi, C., 2018. The role of seawater in interaction of slag and silica fume with cement in low water-to-binder ratio pastes at the early age of hydration. Construct. Build. Mater. 185, 508–518. https://doi.org/10.1016/j.conbuildmat.2018.07.091.

Li, L.G., Chen, X.Q., Chu, S.H., Ouyang, Y., Kwan, A.K.H., 2019. Seawater cement paste: effects of seawater and roles of water film thickness and superplasticizer dosage. Construct. Build. Mater. 229 https://doi.org/10.1016/j.conbuildmat.2019.116862.

Li, P., Li, W., Sun, Z., Shen, L., Sheng, D., 2021. Development of sustainable concrete incorporating seawater : a critical review on cement hydration , microstructure and mechanical strength. Cem. Concr. Compos. 121, 104100 https://doi.org/10.1016/j.cemconcomp.2021.104100.

Li, P., Li, W., Yu, T., Qu, F., Tam, V.W.Y., 2020. Investigation on early-age hydration, mechanical properties and microstructure of seawater sea sand cement mortar. Construct. Build. Mater. 249, 118776 https://doi.org/10.1016/j.conbuildmat.2020.118776.

Li, Q., Geng, H., Shui, Z., Huang, Y., 2015. Effect of metakaolin addition and seawater mixing on the properties and hydration of concrete. Appl. Clay Sci. 115, 51–60. https://doi.org/10.1016/j.clay.2015.06.043.

Liu, Jun, Fan, X., Liu, Jiaying, Jin, H., Zhu, J., Liu, W., 2021. Investigation on mechanical and micro properties of concrete incorporating seawater and sea sand in carbonized environment. Construct. Build. Mater. 307, 124986 https://doi.org/10.1016/j.conbuildmat.2021.124986.

Lothenbach, B., Durdzinski, P., De Weerdt, K., 2016. Thermogravimetric analysis. In: Scrivener, K., Snellings, R., Lothenbach, Barbara (Eds.), A Practical Guide to Microstructural Analysis of Cementitious Materials. CRC press, pp. 177–212.

Lu, J., Shen, P., Zhang, Y., Zheng, H., Sun, Y., Poon, C.S., 2021. Early-age and microstructural properties of glass powder blended cement paste: improvement by seawater. Cem. Concr. Compos. 122, 104165 https://doi.org/10.1016/j.cemconcomp.2021.104165.

Ma, G., Li, Z., Wang, L., 2018. Printable properties of cementitious material containing copper tailings for extrusion based 3D printing. Construct. Build. Mater. 162, 613–627. https://doi.org/10.1016/j.conbuildmat.2017.12.051.

Mantellato, S., Palacios, M., Flatt, R.J., 2019. Relating early hydration, specific surface and flow loss of cement pastes. Mater. Struct. Constr. 52, 1–17. https://doi.org/10.1617/s11527-018-1304-y.

Marchon, D., Flatt, R.J., 2015. Mechanisms of Cement Hydration, Science and Technology of Concrete Admixtures. Elsevier Ltd. https://doi.org/10.1016/B978-0-08-100693-1.00008-4.

Marchon, D., Kawashima, S., Bessaies-Bey, H., Mantellato, S., Ng, S., 2018. Hydration and rheology control of concrete for digital fabrication: potential admixtures and cement chemistry. Cement Concr. Res. 112, 96–110. https://doi.org/10.1016/j.cemconres.2018.05.014.

Mechtcherine, V., Bos, F.P., Perrot, A., da Silva, W.R.L., Nerella, V.N., Fataei, S., Wolfs, R. J.M., Sonebi, M., Roussel, N., 2020. Extrusion-based additive manufacturing with cement-based materials – production steps, processes, and their underlying physics: a review. Cement Concr. Res. 132, 106037 https://doi.org/10.1016/j.cemconres.2020.106037.

Mechtcherine, V., Buswell, R., Kloft, H., Bos, F.P., Hack, N., Wolfs, R., Saranjan, J., Nematollahi, B., Ivaniuk, E., Neef, T., 2021. Integrating reinforcement in digital fabrication with concrete: a review and classification framework. Cem. Concr. Compos. 119, 103964 https://doi.org/10.1016/j.cemconcomp.2021.103964.

Meneses, M., Pasqualino, J.C., Céspedes-Sánchez, R., Castells, F., 2010. Alternatives for reducing the environmental impact of the main residue from a desalination plant. J. Ind. Ecol. 14, 512–527. https://doi.org/10.1111/j.1530-9290.2010.00225.x.

Moeini, M.A., Hosseinpoor, M., Yahia, A., 2020. Effectiveness of the rheometric methods to evaluate the build-up of cementitious mortars used for 3D printing. Construct. Build. Mater. 257, 119551 https://doi.org/10.1016/j.conbuildmat.2020.119551.

Mohan, M.K., Rahul, A.V., Van Tittelboom, K., De Schutter, G., 2020. Extrusion-based concrete 3D printing from a material perspective: a state-of-the-art review. Cem. Concr. Compos. 115, 103855 https://doi.org/10.1016/j.cemconcomp.2020.103855.

Montanari, L., Suraneni, P., Tsui-Chang, M., Khatibmasjedi, M., Ebead, U., Weiss, J., Nanni, A., 2019. Hydration, pore solution, and porosity of cementitious pastes made with seawater. J. Mater. Civ. Eng. 31, 04019154 https://doi.org/10.1061/(asce)mt.1943-5533.0002818.

NEN-EN 196-1, 2016. Methods of Testing Cement - Part 1: Determination of Strength.

NEN-EN 196-3, 2016. Methods of Testing Cement - Part 3: Determination of Setting Times and Soundness.

Nerella, V.N., Näther, M., Iqbal, A., Butler, M., Mechtcherine, V., 2019. Inline quantification of extrudability of cementitious materials for digital construction. Cem. Concr. Compos. 95, 260–270. https://doi.org/10.1016/j.cemconcomp.2018.09.015.

Panagopoulos, A., Haralambous, K.J., 2020. Environmental impacts of desalination and brine treatment - challenges and mitigation measures. Mar. Pollut. Bull. 161, 111773 https://doi.org/10.1016/j.marpolbul.2020.111773.

Panda, B., Paul, S.C., Hui, L.J., Tay, Y.W.D., Tan, M.J., 2017. Additive manufacturing of geopolymer for sustainable built environment. J. Clean. Prod. 167, 281–288. https://doi.org/10.1016/j.jclepro.2017.08.165.

Panda, B., Ruan, S., Unluer, C., Tan, M.J., 2019. Improving the 3D printability of high volume fly ash mixtures via the use of nano attapulgite clay. Compos. B Eng. 165, 75–83. https://doi.org/10.1016/j.compositesb.2018.11.109.

Perrot, A., Rangeard, D., Pierre, A., 2016. Structural built-up of cement-based materials used for 3D-printing extrusion techniques. Mater. Struct. 49, 1213–1220. https://doi.org/10.1617/s11527-015-0571-0.

Rahul, A.V., Atul Narayan, S.P., Neithalath, N., Santhanam, M., 2020. A thermodynamic framework for modelling thixotropic yield stress fluids: application to cement pastes. J. Nonnewton. Fluid Mech. 281, 104318 https://doi.org/10.1016/j.jnnfm.2020.104318.

Reiter, L., 2019. Structural Build-Up for Digital Fabrication with Concrete - Materials, Methods and Processes. ETH Zurich. ETH Zurich.

Reiter, L., Wangler, T., Anton, A., Flatt, R.J., 2020. Setting on demand for digital concrete – principles, measurements, chemistry, validation. Cement Concr. Res. 132, 106047 https://doi.org/10.1016/j.cemconres.2020.106047.

Ren, J., Wang, X., Xu, S., Fang, Y., Liu, W., Luo, Q., Han, N., Xing, F., 2021. Effect of polycarboxylate superplasticisers on the fresh properties of cementitious materials mixed with seawater. Construct. Build. Mater. 289, 123143 https://doi.org/10.1016/j.conbuildmat.2021.123143.

Roberts, D.A., Johnston, E.L., Knott, N.A., 2010. Impacts of desalination plant discharges on the marine environment: a critical review of published studies. Water Res. 44, 5117–5128. https://doi.org/10.1016/j.watres.2010.04.036.

Roychand, R., De Silva, S., Law, D., Setunge, S., 2016. High volume fly ash cement composite modified with nano silica, hydrated lime and set accelerator. Mater. Struct. Constr. 49, 1997–2008. https://doi.org/10.1617/s11527-015-0629-z.

Shanahan, N., Sedaghat, A., Zayed, A., 2016. Effect of cement mineralogy on the effectiveness of chloride-based accelerator. Cem. Concr. Compos. 73, 226–234. https://doi.org/10.1016/j.cemconcomp.2016.07.015.

Shi, Z., Geiker, M.R., De Weerdt, K., Østnor, T.A., Lothenbach, B., Winnefeld, F., Skibsted, J., 2017. Role of calcium on chloride binding in hydrated Portland cement–metakaolin–limestone blends. Cement Concr. Res. 95, 205–216. https://doi.org/10.1016/j.cemconres.2017.02.003.

Shi, Z., Shui, Z., Li, Q., Geng, H., 2015. Combined effect of metakaolin and sea water on performance and microstructures of concrete. Construct. Build. Mater. 74, 57–64. https://doi.org/10.1016/j.conbuildmat.2014.10.023.

Sun, Y., Lu, J.X., Poon, C.S., 2022. Strength degradation of seawater-mixed alite pastes: an explanation from statistical nanoindentation perspective. Cement Concr. Res. 152, 106669 https://doi.org/10.1016/j.cemconres.2021.106669.

Tao, Y., Rahul, A.V., Lesage, K., Van Tittelboom, K., Yuan, Y., De Schutter, G., 2021a. Mechanical and microstructural properties of 3D printable concrete in the context of the twin-pipe pumping strategy. Cem. Concr. Compos. 125, 104324 https://doi.org/10.1016/j.cemconcomp.2021.104324.

Tao, Y., Rahul, A.V., Lesage, K., Yuan, Y., Van Tittelboom, K., De Schutter, G., 2021b. Stiffening control of cement-based materials using accelerators in inline mixing processes: possibilities and challenges. Cem. Concr. Compos. 119, 103972 https://doi.org/10.1016/j.cemconcomp.2021.103972.

Tay, Y.W.D., Qian, Y., Tan, M.J., 2019. Printability region for 3D concrete printing using slump and slump flow test. Compos. B Eng. 174, 106968 https://doi.org/10.1016/j.compositesb.2019.106968.

Wang, J., Liu, E., Li, L., 2018. Multiscale investigations on hydration mechanisms in seawater OPC paste. Construct. Build. Mater. 191, 891–903. https://doi.org/10.1016/j.conbuildmat.2018.10.010.

Wang, J., Xie, J., Wang, Y., Liu, Y., Ding, Y., 2020. Rheological properties, compressive strength, hydration products and microstructure of seawater-mixed cement pastes. Cem. Concr. Compos. 114, 103770 https://doi.org/10.1016/j.cemconcomp.2020.103770.

Weng, Y., Li, M., Tan, M.J., Qian, S., 2018. Design 3D printing cementitious materials via Fuller Thompson theory and Marson-Percy model. Construct. Build. Mater. 163, 600–610. https://doi.org/10.1016/j.conbuildmat.2017.12.112.

Wolfs, R.J.M., Bos, F.P., Salet, T.A.M., 2019. Hardened properties of 3D printed concrete: the influence of process parameters on interlayer adhesion. Cement Concr. Res. 119, 132–140. https://doi.org/10.1016/j.cemconres.2019.02.017.

Wolfs, R.J.M., Salet, T.A.M., Roussel, N., 2021. Filament geometry control in extrusion-based additive manufacturing of concrete: the good, the bad and the ugly. Cement Concr. Res. 150, 106615 https://doi.org/10.1016/j.cemconres.2021.106615.

Yuan, Q., Zhou, D., Li, B., Huang, H., Shi, C., 2018. Effect of mineral admixtures on the structural build-up of cement paste. Construct. Build. Mater. 160, 117–126. https://doi.org/10.1016/j.conbuildmat.2017.11.050.

Zingg, A., Winnefeld, F., Holzer, L., Pakusch, J., Becker, S., Figi, R., Gauckler, L., 2009. Interaction of polycarboxylate-based superplasticizers with cements containing different C3A amounts. Cem. Concr. Compos. 31, 153–162. https://doi.org/10.1016/j.cemconcomp.2009.01.005.